Elastohydrodynamic Relaxation of Soft and Deformable Microchannels

Gabriel Guyard,[1,2,3] Frédéric Restagno,[3] and Joshua D. McGraw[1,2,*]
[1]Gulliver CNRS UMR 7083, PSL Research University, ESPCI Paris, 10 rue Vauquelin, 75005 Paris, France
[2]IPGG, 6 rue Jean-Calvin, 75005 Paris, France
[3]Université Paris-Saclay, CNRS, Laboratoire de Physique des Solides, 91405, Orsay, France

(Received 7 July 2022; accepted 12 October 2022; published 9 November 2022)

Hydrodynamic flows in compliant channels are of great interest in physiology and microfluidics. In these situations, elastohydrodynamic coupling leads to (i) a nonlinear pressure-vs-flow-rate relation, strongly affecting the hydraulic resistance; and (ii), because of the compliance-enabled volume storage, a finite relaxation time under a stepwise change in pressure. This latter effect remains relatively unexplored, even while the timescale can vary over a decade in typical situations. In this study we provide time-resolved measurements of the relaxation dynamics for thin and soft, rectangular microfluidic channels. We describe our data using a perturbative lubrication approximation of the Stokes equation coupled to linear elasticity, while taking into account the effect of compliance and resistance of the entrance. The modeling allows us to completely describe all of the experimental results. Our Letter is relevant for any microfluidic scenario wherein a time-dependent driving is applied and provides a first step in the dynamical description of compliant channel networks.

DOI: 10.1103/PhysRevLett.129.204501

To force the movement of fluid through a channel, a pressure drop must be applied across its ends. If the bounding walls of this simple flow domain are compliant, a pressure-induced deformation can strongly affect the flow as compared to the noncompliant case. This elastohydrodynamic (EHD) coupling is often encountered, and the pipe-flow case is referred to as soft hydraulics [1]. Particularly, the flow modification can give a nonlinear pressure-vs-flow-rate relation [2,3], with the flow resistance changing by an order of magnitude or more. Upon a pressure change, however, the relaxation to a new deformation profile is not instantaneous. The pipe thus settles into a new configuration over a little-investigated, pressure-dependent timescale at the focus of this Letter.

Elastohydrodynamics was historically studied in the context of lubrication of rough, solid contacts [4–6], often for heavy mechanical applications and remains a key ingredient in modern tribology [7]. Conversely, the lubrication of soft materials has attracted increasing attention in the last decades [8–12] due in part to its relevance in biology and microtechnologies. Examples include joint lubrication [13], eyelid wiper mechanics [14], and the deformation of blood vessels under flow-induced pressure [15–19]. At microscales, EHD interactions may affect the transport of blood cells [20] because of the emergent lift forces arising from the fluid-mediated soft-substrate deformation [21].

Concerning soft technologies, microfluidics is of significant interest [22]. Indeed, microchannels are typically made with soft elastomers—e.g., polydimethylsiloxane (PDMS)—allowing for fast prototyping, design fidelity, and transparency [23,24]. Compliance is a key attribute for applications such as organ on a chip [25,26] or wearable technologies [27,28]. Targeted actuation of deformable pipes also enables the generation and manipulation of flows at the scale of a single channel [29–31], or in complex networks [32] as in the plant kingdom [33]. Finally, soft components can be used as pressure-controlled valves serving as building blocks for the logic gate components in state-of-the-art microdevices [34–36].

While many soft-hydraulics studies focus on the steady state, compliance is also expected to have dynamic effects. This deformability leads to volume storage capacity [37], schematically indicated in Fig. 1(a), which in addition to changing the resistance of a narrow channel, implies a characteristic response time of the system by analogy with electronics [38,39], see Fig. 1(b). This dynamic response was used for example to attenuate parasitic fluctuations in syringe-pump driven flows [40], and limits the production rate in stop-flow lithography [41].

With dynamical aspects of soft hydraulics already finding applications, it is imperative to characterize the temporal response of compliant microchannels. Here we experimentally and theoretically investigate the response of thin, soft microfluidic channels to stepwise pressure perturbations. We use an EHD model in the lubrication limit applied to such devices. As previously [2,3,42], this approach allows us to rationalize the nonlinear relation between pressure and flow rate. Performing a perturbation analysis and, crucially, specifying the capacitance and resistance of the peripheral components, the pressure-dependent relaxation dynamics of the entire experimental

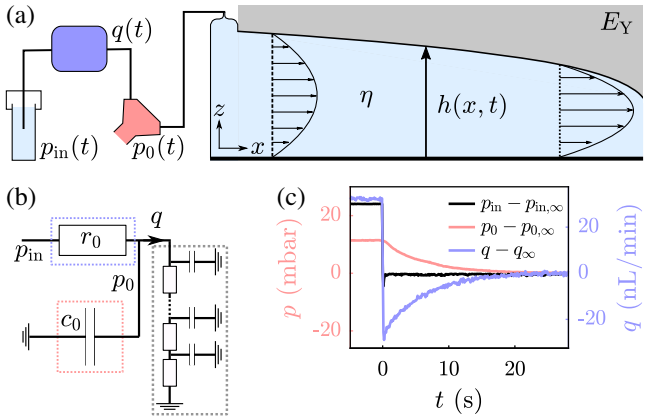

FIG. 1. (a) Schematics of the microfluidic setup, including a flow sensor, a pressure sensor and a soft channel. (b) Equivalent electronic circuit, the flow sensor modeled as an ideal resistance r_0, the pressure sensor as a capacitance c_0, and the soft channel as a series of infinitesimal resistances and capacities as in a transmission line. (c) Shifted, imposed p_{in}, and measured p_0 and q as a function of t, with long-time values of $p_{in,\infty} = 1301$ mbar, $p_{0,\infty} = 862$ mbar, and $q_\infty = 1058$ nL/ min.

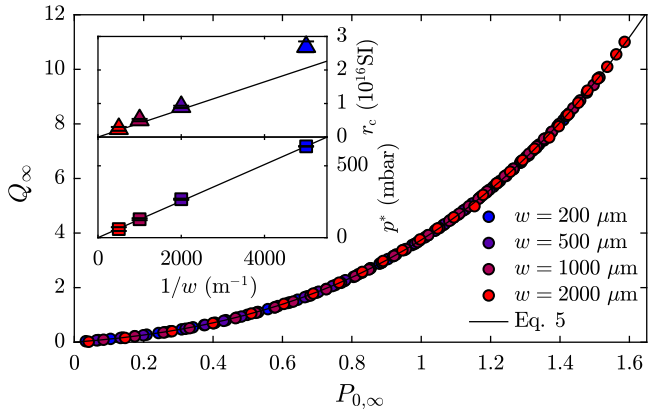

FIG. 2. Dimensionless steady-state flow rate $Q_\infty = q_\infty r_c/p^*$ as a function of the dimensionless steady-state inlet pressure $P_{0,\infty} = p_{0,\infty}/p^*$ for channels of the indicated widths. The solid line indicates the model of Eq. (5). Error bars are smaller than symbol size; insets show fitting parameters p^* and r_c.

system are revealed. Our approach includes an asymptotic analysis of the general high- and low-pressure limits, along with the full crossover requiring complete specification of the microsystem.

The microfluidic chips used here consisted of rectangular channels with length $L = 4.0$ cm between the inlet and outlet centers of radius $d_c = 1.0$ mm (cf. the Supplemental Material, Sec. I [43], for a full list of symbols). The channel widths were $w = \{200, 500, 1000, 2000\}$ μm, with uncertainty of order a few micrometers, and undeformed heights $h_0 = 5.0 \pm 0.1$ μm. The molds were characterized with a mechanical profilometer (Bruker Dektak). Liquid reservoirs were connected to chips using tubing with negligible hydraulic resistance and compliance (PEEK, IDEX 1581, ID 0.25 mm, OD 1/32," length *ca.* 50 cm). Microchannels were fabricated [23] from PDMS (Momentive RT 615 A & B) including 10 wt.% cross-linker, and cured at 170 °C for 15 min.

Flow and pressure sensors (Elveflow MFS1 and MPS2) provided time-resolved measurements of the flow rate q and pressure p_0, relative to atmospheric pressure, at the chip inlet. Ultrapure water (Milli-Q, 18.2 MΩ cm, viscosity $\eta = 1.00 \pm 0.02$ mPa s) at room temperature was driven using a pressure controller (Elveflow OB1 mk3+), with constant pressure, p_{in}, imposed across the input sensors and the microchannel, see Fig. 1(a). After reaching steady state, p_{in} was suddenly dropped and the temporal responses $q(t)$ and $p_0(t)$ recorded until a new steady state was reached; a selection of raw data is also shown in the Supplemental Material, Sec. II [43].

Figure 1(c) shows a set of recorded signals for $p_{in}(t)$, $p_0(t)$, and $q(t)$ after a single pressure drop. Each signal is shifted to its long-time, steady value, denoted $p_{in,\infty}$, $p_{0,\infty}$, and q_∞, respectively. While p_{in} varies on a timescale of just 0.1 s, p_0 and q reach new steady states after a much longer transient time, τ_t, of order 10 s, depending on the initial input pressure and channel geometry. In the following we study the dependence of q_∞ and τ_t, on $p_{0,\infty}$ and w.

In Fig. 2 is shown the scaled relation between the dimensionless, steady-state flow rate Q_∞ and pressure $P_{0,\infty}$ for all of the chip geometries used here. While the raw data are shown in the Supplemental Material, Sec. III [43], here the pressure is normalized by the natural scale $p^* = E^* h_0/w$. The semi-infinite slab case [2,44] gives $E^* \approx E_Y/0.5427(1-\nu^2)$, where ν and E_Y are the Poisson ratio and Young's modulus of the material [45]. The flow rate is normalized by p^*/r_c, with $r_c = 12\eta L/wh_0^3$ the hydraulic resistance of an undeformed rectangular channel [46]. Such a normalization gives a single master curve after adjusting the data to the fitting parameters for each chip, p^* and r_c. These latter follow the expected scaling with w, as seen in the insets, the top one with no fitting parameter on the line. The slope of the line of the bottom inset finally gives a measurement of $E_Y = 1.07 \pm 0.03$ MPa, consistent with the typical value for this PDMS [47]. In contrast to rigid pipe flow [46,48], the flow-rate response of these channels is highly nonlinear. Indeed, when the pressure is increased, the channel's resistance decreases due to its dilation.

Considering the dynamics, in Fig. 3 is shown $p_0 - p_{0,\infty}$ as a function of time in a 200 μm-wide channel for several $p_{0,\infty}$; straight lines in semi-log axis indicate exponential relaxations, allowing a precise determination of τ_t. The inset of Fig. 3 thus shows the characteristic time τ_t as a function of $p_{0,\infty}$, the relaxation time decreasing by a factor of 5 across the accessed range of $p_{0,\infty}$. As deformation allows the channel to store a pressure-dependent fluid

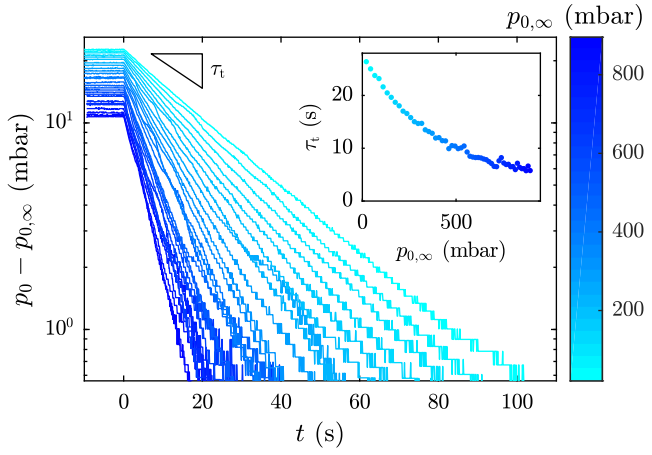

FIG. 3. Inlet pressure $p_0 - p_{0,\infty}$ as a function of time t in a 200 μm-wide channel, the color bar indicating $p_{0,\infty}$. The inset shows the exponential relaxation time, obtained from best fits, as a function of $p_{0,\infty}$. Error bars are smaller than symbol size.

volume, a microfluidic chip is a liquid-storage capacitor. Furthermore, the channels exhibit resistance, so that they are RC fluidic circuits [38,46]. To rationalize the nonlinearity of q_∞ with $p_{0,\infty}$, as well as the dependence of τ_t on $p_{0,\infty}$, we propose the following elastohydrodynamic model.

Considering the one dimensional limit since $h_0 \ll w \ll L$, we denote $h(x,t)$ the time-dependent height of the microchannel along the center line and along the flow direction x and $p(x,t)$ the pressure field within the channel. In the lubrication limit, the Reynolds equation [49] expresses conservation of volume for incompressible, Newtonian fluids:

$$\partial_t h = \frac{1}{12\eta}\partial_x(h^3\partial_x p). \tag{1}$$

Since the former equation introduces the unknown fields $h(x,t)$ and $p(x,t)$, an elastic model is needed to connect the height profile to the pressure field. Even though the height profile varies in both the streamwise x and transverse y directions, as detailed by Christov and co-workers [3,42], we consider a local, linear elastic response of the surrounding material along the center line:

$$h(x,t) = h_0 + \frac{w}{E^*}p(x,t), \tag{2}$$

neglecting possible viscous losses in the PDMS [50].

To close the problem, we consider the boundary conditions. At the outlet we simply have $p(L,t) = 0$. At the inlet, we account for the peripheral sensors. Using the classic analogy between microfluidics and electronics [38,39,46], the setup is akin to the circuit depicted in Fig. 1(b). The flow sensor, composed of a thin hard glass capillary, is modeled as an ideal resistance r_0. The pressure sensor, including deformable parts, is modeled with a negligibly resistant capacity $c_0 = d\Omega/dp_0$, where Ω is the volume of fluid stored in the sensor with pressure playing the role of the electric potential. Flux conservation then reads as the electrical current flowing through a resistance and the discharge current of a capacitor on one side, and the current at the entrance of a nonlinear transmission line (cf. Ref. [51]) on the other:

$$\frac{p_{\text{in}} - p_0}{r_0} - c_0\frac{dp_0}{dt} = \left(-\frac{wh^3}{12\eta}\partial_x p\right)\bigg|_{x=0}. \tag{3}$$

Nondimensionalizing, we take $h = h_0 H$, $x = LX$, $t = \tau_c T$ with $\tau_c = 12\eta w L^2/h_0^3 E^*$ as in Ref. [41], and pressures take the form $p = p^* P$. Combining Eqs. (1) and (2), we obtain the elastohydrodynamic equation for the pressure field within the chip:

$$\partial_T P = \partial_X[(1+P)^3\partial_X P]. \tag{4}$$

In the steady state, with a constant inlet pressure $P_{0,\infty}$ and null outlet pressure, a single integration of Eq. (4) gives $P_\infty(X) = [(1-X)((1+P_{0,\infty})^4 - 1) + 1]^{1/4} - 1$. From this pressure profile, we compute the steady flux Q_∞ using the square-bracketed term of Eq. (4):

$$Q_\infty = \frac{1}{4}[(1+P_{0,\infty})^4 - 1] = \frac{1}{4}\Pi, \tag{5}$$

having introduced $\Pi = (1+P_{0,\infty})^4 - 1$. Equation (5) has a similar form to the expressions given previously [3,42], and we note the excellent agreement between this model (black line) and the data of Fig. 2.

Addressing the time-dependent problem now, we linearize Eq. (4), introducing $\delta P(X,T) = P(X,T) - P_\infty(X)$. At $\mathcal{O}(\delta P^1)$ and after the linear change of variables $\tilde{X} = (1-X)\Pi + 1$ and $\tilde{T} = \Pi^2 T$, we obtain

$$\partial_{\tilde{T}}\delta P = \partial^2_{\tilde{X}}[\tilde{X}^{3/4}\delta P]. \tag{6}$$

Looking for separable solutions of Eq. (6), we propose $\delta P(\tilde{X},\tilde{T}) = A(\tilde{X})B(\tilde{T})$. Using the boundary condition for $\delta P = 0$ at $\tilde{X} = 1$, we obtain $B_\lambda(\tilde{T}) = \exp(-\lambda\tilde{T})$, confirming the experimentally observed exponential pressure decay; determining the eigenvalues λ remains. For the spatial part, we have [52] $A_\lambda(\tilde{X}) = \alpha_\lambda\tilde{X}^{-1/4}\mathcal{C}_{\frac{4}{5}}((8\sqrt{\lambda}/5)\tilde{X}^{5/8})$, where α_λ is an integration constant. The function $\mathcal{C}_\nu$ is a linear combination of Bessel functions, here of the form $\mathcal{C}_\nu(x) = Y_{\frac{4}{5}}(8\sqrt{\lambda}/5)J_\nu(x) - J_{\frac{4}{5}}(8\sqrt{\lambda}/5)Y_\nu(x)$, satisfying $p(L,t) = 0$.

For the boundary condition at the channel entrance, the full solution $P_\infty(X) + \delta P(\tilde{X},\tilde{T})$ can be injected into the dimensionless version of Eq. (3). Such a substitution gives a constraining equation on the eigenvalues, λ, after evaluation at $\tilde{X}_0 = 1 + \Pi$, i.e., the channel entrance

$$\frac{1}{\mathcal{R}\tilde{X}_0^{3/8}}\left(\mathcal{T}\sqrt{\lambda}\Pi - \frac{1}{\sqrt{\lambda}\Pi}\right) = \frac{\mathcal{C}_{-\frac{1}{5}}(\frac{8\sqrt{\lambda}}{5}\tilde{X}_0^{5/8})}{\mathcal{C}_{\frac{4}{5}}(\frac{8\sqrt{\lambda}}{5}\tilde{X}_0^{5/8})}, \quad (7)$$

with $\mathcal{R} = r_0/r_c$ and $\mathcal{T} = \tau_0/\tau_c$, where $\tau_0 = r_0 c_0$ is the inlet timescale. Recalling that the experimentally measured pressure relaxations of Fig. 3 are well described by simple exponential decays, and denoting λ_s smallest eigenvalue satisfying Eq. (7), the experimentally measured timescale is then assumed to be

$$\frac{\tau_t}{\tau_c} = \frac{1}{\Pi^2}\lambda_s^{-1}(\Pi, \mathcal{R}, \mathcal{T}), \quad (8)$$

in accordance with the definition of $\tilde{T}$. This relation shows that the relaxation timescale is a function of the pressure through Π, and in particular depends on the details of the input resistance and capacitance, here reflected through the dimensionless variables $\mathcal{R}$ and $\mathcal{T}$.

We are not aware of analytic solutions for Eq. (7); nevertheless, the asymptotic behavior can be assessed. At low pressure, there is no significant channel deformation ($p_0 \ll p^*$) such that the chip is an ideal resistance. We do not expect the relaxation time to be pressure dependent in this limit. Conversely, at high pressure, the deformation makes the resistance of the chip pressure dependent. According to Eq. (5), we have a chip resistance, and thus a timescale proportional to $P_{0,\infty}^{-3}$. We thus look for asymptotic, power-law solutions to Eq. (7), $\lambda_s \approx \beta^2\Pi^\gamma$, with constant β and γ. Using asymptotic developments of the Bessel functions (Supplemental Material, Sec. IV [43]), we confirm the power laws

$$\frac{\tau_t}{\tau_c} = \frac{1}{\beta^2} : \Pi \ll 1, \quad (9)$$

$$\frac{\tau_t}{\tau_c} = \frac{1}{\beta^2 P_{0,\infty}^3} : \Pi \gg 1. \quad (10)$$

Here, β satisfies $\mathcal{T}\beta^2 - \mathcal{R}\beta\cot(\beta) - 1 = 0$ and $\mathcal{T}\beta/\mathcal{R} = J_{-\frac{1}{5}}(8\beta/5)/J_{\frac{4}{5}}(8\beta/5)$ in the low- and high-Π limits; we also note that $\mathcal{T}$ and $\mathcal{R}$ may differ in these limits.

For intermediate pressures, Eq. (8) is solved numerically for prescribed values of $\{\Pi, \mathcal{R}, \mathcal{T}\}$, thus necessitating characterizations of the input r_0 and c_0. The former was determined by measuring $p_{\text{in},\infty}$, versus q_∞ in the presence of the flow meter only. The data (Supplemental Material, Sec. V [43]) are well described by a straight line, giving $r_0 = 2.50 \pm 0.01$ kPa s/nL, consistent with a rigid glass capillary of diameter 25 μm and length 2.4 cm filled with water of viscosity $\eta = 1.0$ mPa s/nL [46]. The value of c_0 is assessed by plugging the circuit at the pressure sensor outlet and removing the microchannel, assuming that the resulting relaxation time satisfies $\tau_0 = r_0 c_0$. The inset of Fig. 4 shows τ_0 as a function of $p_{0,\infty}$ for such a plugged experiment, indicating a clearly nonlinear inlet capacity.

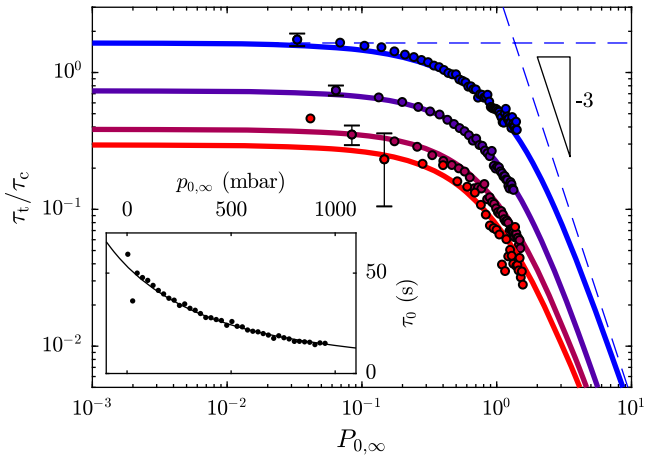

FIG. 4. Normalised transient relaxation time as a function of dimensionless steady-state pressure of different widths, color map as in Fig. 2. Single, typical error bars are shown for each dataset. Solid lines represent numerical solutions of the model of Eq. (8) using ideal input resistance and an ideal-gas-like input capacitance, with dashed lines the asymptotic developments [Eqs. (9) and (10)], for the 200 μm-wide channel. Inset: τ_0 as a function of $p_{0,\infty}$ for the plugged experiment. Error bars are smaller than symbol size. The solid line is a fit to the model including an ideal gas capacitance.

Assuming that the nontrivial capacity at the channel inlet is dominated by trapped air, we use the ideal gas law to estimate $c_0 = c_1(1 + p_{0,\infty}/p_{\text{atm}})^{-2} + c_2$. Here $p_{\text{atm}} = 101$ kPa is the atmospheric pressure, $c_1 = \Omega_a/p_{\text{atm}}$, with Ω_a the trapped air volume at atmospheric pressure. The second term, c_2, describes any other linear capacity, is assumed to be connected to the atmosphere and is thus in parallel with c_1. The solid line in the inset provides an excellent fit using this ideal-gas-like inlet capacity, with $c_1 = 20.9 \pm 0.1$ and $c_2 = 0.2 \pm 0.1$ nL kPa$^{-1} \ll c_1$. The value of c_1 corresponds to a resting gas volume of 2.1 μL, which compares reasonably to the internal volume of the pressure sensor of 7.5 μL as provided by the manufacturer.

Making a full test of the model for our complete microfluidic system, Fig. 4 shows the normalized relaxation time τ_t/τ_c as a function of $P_{0,\infty}$ for all channel widths used here. The solid lines represent the solution of the problem [Eqs. (7) and (8)], where Eq. (7) is solved numerically using the aforementioned ideal resistance value and the ideal-gas, pressure-dependent capacitance. For these data the best-fitting values were $c_1 = 8.6 \pm 0.4$ and $c_2 = 2.1 \pm 0.2$ nL kPa^{-1}, respectively. Here the larger value of c_2 corresponds well to the linear capacity of the circular channel inlet, approximated by $c_2 \approx d_c^3/E^* \approx 1$ nL kPa^{-1}. The smaller value of c_1 suggests that less air was trapped compared to the calibration. We additionally show the asymptotic behaviors, where the equations for

prefactors β were solved graphically using the limiting values of $\mathcal{T}$ and $\mathcal{R}$. Our model describes the data well over more than one decade of normalized pressures and four chip geometries, all fitted using the same c_1 and c_2, the experiments having been performed sequentially.

In conclusion, we have used time-resolved pressure and flow-rate measurements to characterize the relaxation dynamics of compliant microfluidic channels. We recover the well-known, quartic pressure-vs-flow-rate relation for straight, rectangular channels. Additionally, we measured a full series of pressure-dependent relaxation timescales resulting from stepwise pressure perturbations in a series of chip widths. Our main results are (i) the chip inlet impedance cannot be neglected; and (ii), there is a strong pressure dependence on the relaxation timescale that cannot be simply predicted by dimensional analysis. A perturbation analysis of the lubrication-approximated microflow problem, coupled to a linear elasticity of the channel walls and considering the inlet impedance, accounts fully for the measured timescales. In a more general context, ours is a simple unit of any potential compliant flow network. Our analysis could thus be exploited in a broad range of microbiological, and microtechnological contexts already finding applications.

The authors thank Ivan C. Christov, Thomas Salez, Stéphane Jouenne, Alexandre Vilquin and Andreas Carlson for fruitful discussions. The authors benefited from the financial support of the Agence Nationale de la Recherche (ANR) under the CoPinS (ANR-19CE06-0021) grant, and of the Institut Pierre-Gilles de Gennes (Equipex ANR-10-EQPX-34 and Labex ANR-10-LABX-31), PSL Research University (Idex ANR-10-IDEX-0001-02). Total Energies is also gratefully acknowledged for financial support under contract TOTAL DS3700–CNRS 2019200804.

*joshua.mcgraw@cnrs.fr

[1] I. C. Christov, Soft hydraulics: from Newtonian to complex fluid flows through compliant conduits, J. Phys. Condens. Matter **34**, 063001 (2022).
[2] T. Gervais, J. El-Ali, A. Günther, and K. F. Jensen, Flow-induced deformation of shallow microfluidic channels, Lab Chip **6**, 500 (2006).
[3] I. C. Christov, V. Cognet, T. C. Shidhore, and H. A. Stone, Flow rate–pressure drop relation for deformable shallow microfluidic channels, J. Fluid Mech. **841**, 267 (2018).
[4] R. Stribeck, *Kugellager für beliebige Belastungen* (Springer, New York, 1901).
[5] R. Gohar and A. Cameron, Optical measurement of oil film thickness under elasto-hydrodynamic lubrication, Nature (London) **200**, 458 (1963).
[6] K. Johnson, J. Greenwood, and S. Poon, A simple theory of asperity contact in elastohydro-dynamic lubrication, Wear **19**, 91 (1972).
[7] J. Hansen, M. Björling, and R. Larsson, Lubricant film formation in rough surface non-conformal conjunctions subjected to GPa pressures and high slide-to-roll ratios, Sci. Rep. **10**, 22250 (2020).
[8] S. Leroy and E. Charlaix, Hydrodynamic interactions for the measurement of thin film elastic properties, J. Fluid Mech. **674**, 389 (2011).
[9] Y. Wang, C. Dhong, and J. Frechette, Out-of-Contact Elastohydrodynamic Deformation due to Lubrication Forces, Phys. Rev. Lett. **115**, 248302 (2015).
[10] B. Saintyves, T. Jules, T. Salez, and L. Mahadevan, Self-sustained lift and low friction via soft lubrication, Proc. Natl. Acad. Sci. U.S.A. **113**, 5847 (2016).
[11] Z. Zhang, V. Bertin, M. Arshad, E. Raphaël, T. Salez, and A. Maali, Direct Measurement of the Elastohydrodynamic Lift Force at the Nanoscale, Phys. Rev. Lett. **124**, 054502 (2020).
[12] V. Bertin, Y. Amarouchene, E. Raphaël, and T. Salez, Soft-lubrication interactions between a rigid sphere and an elastic wall, J. Fluid Mech. **933**, A23 (2022).
[13] S. Jahn, J. Seror, and J. Klein, Lubrication of articular cartilage, Annu. Rev. Biomed. Eng. **18**, 235 (2016).
[14] M. Jones, G. Fulford, C. Please, D. McElwain, and M. J. Collins, Elastohydrodynamics of the Eyelid Wiper, Bull. Math. Biol. **70**, 323 (2008).
[15] K. Perktold and G. Rappitsch, Computer simulation of local blood flow and vessel mechanics in a compliant carotid artery bifurcation model, J. Biomech. **28**, 845 (1995).
[16] C. A. Figueroa, I. E. Vignon-Clementel, K. E. Jansen, T. J. Hughes, and C. A. Taylor, A coupled momentum method for modeling blood flow in three-dimensional deformable arteries, Comput. Methods Appl. Mech. Eng. **195**, 5685 (2006).
[17] M. Heil and A. L. Hazel, Fluid-structure interaction in internal physiological flows, Annu. Rev. Fluid Mech. **43**, 141 (2011).
[18] M. Hirschhorn, V. Tchantchaleishvili, R. Stevens, J. Rossano, and A. Throckmorton, Fluid–structure interaction modeling in cardiovascular medicine—A systematic review 2017–2019, Medical Engineering and Physics **78**, 1 (2020).
[19] C. A. Taylor, T. J. Hughes, and C. K. Zarins, Finite element modeling of three-dimensional pulsatile flow in the abdominal aorta: relevance to atherosclerosis, Ann. Biomed. Eng. **26**, 975 (1998).
[20] H. S. Davies, D. Débarre, N. El Amri, C. Verdier, R. P. Richter, and L. Bureau, Elastohydrodynamic Lift at a Soft Wall, Phys. Rev. Lett. **120**, 198001 (2018).
[21] J. M. Skotheim and L. Mahadevan, Soft Lubrication, Phys. Rev. Lett. **92**, 245509 (2004).
[22] H. Xia, J. Wu, J. Zheng, J. Zhang, and Z. Wang, Nonlinear microfluidics: device physics, functions, and applications, Lab Chip **21**, 1241 (2021).
[23] Y. Xia and G. M. Whitesides, Soft Lithography, Annu. Rev. Mater. Sci. **28**, 153 (1998).
[24] K. Raj M. and S. Chakraborty, PDMS microfluidics: A mini review, J. Appl. Polym. Sci. **137**, 48958 (2020).
[25] D. Huh, B. D. Matthews, A. Mammoto, M. Montoya-Zavala, H. Y. Hsin, and D. E. Ingber, Reconstituting organ-level lung functions on a chip, Science **328**, 1662 (2010).

[26] J. U. Lind, T. A. Busbee, A. D. Valentine, F. S. Pasqualini, H. Yuan, M. Yadid, S.-J. Park, A. Kotikian, A. P. Nesmith, P. H. Campbell *et al.*, Instrumented cardiac microphysiological devices via multimaterial three-dimensional printing, Nat. Mater. **16**, 303 (2017).

[27] S. Xu, Y. Zhang, L. Jia, K. E. Mathewson, K.-I. Jang, J. Kim, H. Fu, X. Huang, P. Chava, R. Wang *et al.*, Soft microfluidic assemblies of sensors, circuits, and radios for the skin, Science **344**, 70 (2014).

[28] J. C. Yeo, K. Kenry, and C. T. Lim, Emergence of microfluidic wearable technologies, Lab Chip **16**, 4082 (2016).

[29] D. P. Holmes, B. Tavakol, G. Froehlicher, and H. A. Stone, Control and manipulation of microfluidic flow via elastic deformations, Soft Matter **9**, 7049 (2013).

[30] F. J. Meigel, P. Cha, M. P. Brenner, and K. Alim, Robust Increase in Supply by Vessel Dilation in Globally Coupled Microvasculature, Phys. Rev. Lett. **123**, 228103 (2019).

[31] E. Virot, V. Spandan, L. Niu, W. M. van Rees, and L. Mahadevan, Elastohydrodynamic Scaling Law for Heart Rates, Phys. Rev. Lett. **125**, 058102 (2020).

[32] J. W. Rocks, A. J. Liu, and E. Katifori, Hidden Topological Structure of Flow Network Functionality, Phys. Rev. Lett. **126**, 028102 (2021).

[33] K. Park, A. Tixier, M. Paludan, E. Østergaard, M. Zwieniecki, and K. H. Jensen, Fluid-structure interactions enable passive flow control in real and biomimetic plants, Phys. Rev. Fluids **6**, 123102 (2021).

[34] B. Mosadegh, C.-H. Kuo, Y.-C. Tung, Y.-s. Torisawa, T. Bersano-Begey, H. Tavana, and S. Takayama, Integrated elastomeric components for autonomous regulation of sequential and oscillatory flow switching in microfluidic devices, Nat. Phys. **6**, 433 (2010).

[35] J. A. Weaver, J. Melin, D. Stark, S. R. Quake, and M. A. Horowitz, Static control logic for microfluidic devices using pressure-gain valves, Nat. Phys. **6**, 218 (2010).

[36] P. N. Duncan, T. V. Nguyen, and E. E. Hui, Pneumatic oscillator circuits for timing and control of integrated microfluidics, Proc. Natl. Acad. Sci. U.S.A. **110**, 18104 (2013).

[37] D. C. Leslie, C. J. Easley, E. Seker, J. M. Karlinsey, M. Utz, M. R. Begley, and J. P. Landers, Frequency-specific flow control in microfluidic circuits with passive elastomeric features, Nat. Phys. **5**, 231 (2009).

[38] K. W. Oh, K. Lee, B. Ahn, and E. P. Furlani, Design of pressure-driven microfluidic networks using electric circuit analogy, Lab Chip **12**, 515 (2012).

[39] D. J. Preston, P. Rothemund, H. J. Jiang, M. P. Nemitz, J. Rawson, Z. Suo, and G. M. Whitesides, Digital logic for soft devices, Proc. Natl. Acad. Sci. U.S.A. **116**, 7750 (2019).

[40] Z. Jiao, J. Zhao, Z. Chao, Z. You, and J. Zhao, Digital microfluidic platform for automated detection of human chorionic gonadotropin, Microfluid. Nanofluid. **23**, 1 (2019).

[41] D. Dendukuri, S. S. Gu, D. C. Pregibon, T. A. Hatton, and P. S. Doyle, Stop-flow lithography in a microfluidic device, Lab Chip **7**, 818 (2007).

[42] X. Wang and I. C. Christov, Theory of the flow-induced deformation of shallow compliant microchannels with thick walls, Proc. R. Soc. A **475**, 20190513 (2019).

[43] See Supplemental Material at http://link.aps.org/supplemental/10.1103/PhysRevLett.129.204501 for a full list of symbols, a selection of raw data for the time dependence of flow rate and pressures; asymptotic analysis of the eigenvalue equation; and flow sensor calibration data.

[44] X. Wang and I. C. Christov, Reduced models of unidirectional flows in compliant rectangular ducts at finite Reynolds number, Phys. Fluids **33**, 102004 (2021).

[45] We note that the infinitely thick limit is expected when the thickness of the upper, flexible wall is roughly twice the width of the channel, which is always the case here. With the reported value [53] of $\nu = 0.495$, we have $E^* \approx 2.44 E_Y$.

[46] H. Bruus, *Theoretical Microfluidics* (Oxford University Press, New York, 2008).

[47] A. I. Panou, K. G. Papadokostaki, P. A. Tarantili, and M. Sanopoulou, Effect of hydrophilic inclusions on PDMS crosslinking reaction and its interrelation with mechanical and water sorption properties of cured films, Eur. Polym. J. **49**, 1803 (2013).

[48] P. Tabeling, *Introduction to Microfluidics*, 1st ed. (Oxford University Press, New York, 2010).

[49] A. Oron, S. H. Davis, and S. G. Bankoff, Long-scale evolution of thin liquid films, Rev. Mod. Phys. **69**, 931 (1997).

[50] V. Placet and P. Delobelle, Mechanical properties of bulk polydimethylsiloxane for microfluidics over a large range of frequencies and aging times, J. Micromech. Microeng. **25**, 035009 (2015).

[51] B. K. Wunderlich, U. A. Kleßinger, and A. R. Bausch, Diffusive spreading of time-dependent pressures in elastic microfluidic devices, Lab Chip **10**, 1025 (2010).

[52] DLMF, NIST digital library of mathematical functions, http://dlmf.nist.gov/, Release 1.1.5 of 2022-03-15, f. W. J. Olver, A. B. Olde Daalhuis, D. W. Lozier, B. I. Schneider, R. F. Boisvert, C. W. Clark, B. R. Miller, B. V. Saunders, H. S. Cohl, and M. A. McClain, eds.

[53] A. Müller, M. C. Wapler, and U. Wallrabe, A quick and accurate method to determine the Poisson's ratio and the coefficient of thermal expansion of PDMS, Soft Matter **15**, 779 (2019).